

# Chern number spectrum of ultra-cold fermions in optical lattices tuned independently via artificial magnetic, Zeeman and spin-orbit fields

Man Hon Yau and C. A. R. Sá de Melo

*School of Physics, Georgia Institute of Technology, Atlanta, 30332, USA*

(Dated: November 2, 2018)

We discuss the Chern number spectrum of ultra-cold fermions in square optical lattices as a function of artificial magnetic, Zeeman and spin-orbit fields that can be tuned independently. We show the existence of topological quantum phase transitions induced by Zeeman and spin-orbit fields, where the total number and chirality of edge states change for fixed magnetic flux ratio, thus leading to topological-insulator phases which are different from those found at zero Zeeman and spin-orbit fields. We construct phase diagrams of chemical potential versus Zeeman field or spin-orbit coupling and characterize all insulating phases by their topological invariants. Lastly, we obtain a staircase structure in the filling factor versus chemical potential for various Zeeman and spin-orbit fields, showing the existence of incompressible states at rational filling factors derived from a generalized Diophantine equation.

Ultra-cold fermions loaded in optical lattices have become ideal systems to study related electronic phase diagrams and transport properties, because they provide a clean and well controlled playground to change various lattice parameters and external fields at the turn of a knob. It is now possible to create artificial magnetic fields [1, 2] in optical lattices that mimic electronic materials exhibiting integer [3] and fractional [4] quantum Hall effects. The synthetic magnetic flux values reached are sufficiently large to allow for the experimental exploration of the intricacies of the Harper's model [5] and the Hofstadter butterfly [6], such as the experimental determination of Chern numbers [7]. Furthermore the creation of artificial spin-orbit coupling for ultra-cold atoms [8] allows for the simulation of electronic materials exhibiting the quantum spin-Hall effect [9–11].

For ultra-cold fermions, artificial magnetic fields allow for studies of topological insulators that break time reversal symmetry, such as quantum hall systems, while artificial spin-orbit fields allow for studies of topological insulators that do not break time reversal symmetry, such as quantum spin-Hall systems. Both types of topological insulators are characterized by Berry curvatures and Chern numbers, which have been measured using time of flight techniques [12], inspired by theoretical proposals [13, 14], and using dynamics of the center of mass of the atomic cloud [15], also motivated by theoretical work [16, 17]. However, studies of ultra-cold fermions can go way beyond the quantum simulation of topological insulators under typical condensed matter conditions. The independent tunability of artificial magnetic, spin-orbit and Zeeman fields in cold atoms is possible via the combination of experimental techniques that produce artificial magnetic fluxes without using internal states, such as laser assisted tunneling [1, 2], or that produce spin-orbit and Zeeman fields using internal states, such as Raman processes [8] or radio-frequency chips [18].

In this paper, we study the interplay of artificial magnetic, spin-orbit and Zeeman fields and their effects on topological insulators in regimes that cannot be reached in condensed matter physics. We analyse the Chern

number spectrum of fermionic atoms with two internal states, such as,  $^6\text{Li}$  or  $^{40}\text{K}$ , and show that topological quantum phase transitions are induced by Zeeman and spin-orbit fields at constant magnetic flux. Finally, we construct phase diagrams of chemical potential versus Zeeman field or spin-orbit coupling and characterize all insulating phases by their topological invariants.

*Hamiltonian:* We begin our investigation by writing the first quantization Hamiltonian matrix for ultra-cold fermions in a two-dimensional square optical lattice as

$$\hat{H} = \begin{pmatrix} \varepsilon_{\uparrow}(\hat{\mathbf{k}}) & -h_x \\ -h_x & \varepsilon_{\downarrow}(\hat{\mathbf{k}}) \end{pmatrix}, \quad (1)$$

where  $\varepsilon_{\uparrow}(\hat{\mathbf{k}}) = -2t\{\cos[(\hat{k}_x - k_T)a] + \cos[(\hat{k}_y - \mathcal{A}_y)a]\}$  corresponds to the spin-up ( $\uparrow$ ) kinetic energy and  $\varepsilon_{\downarrow}(\hat{\mathbf{k}}) = -2t\{\cos[(\hat{k}_x + k_T)a] + \cos[(\hat{k}_y - \mathcal{A}_y)a]\}$  corresponds to the spin-down ( $\downarrow$ ) kinetic energy. Here,  $t$  is the hopping amplitude,  $a$  is the lattice spacing,  $k_T$  is a spin-dependent momentum transfer characterizing an artificial unidirectional (one-dimensional) spin-orbit coupling, and  $\mathcal{A}_y = eHx/\hbar c$  plays the role of the  $y$ -component of an artificial vector potential, where  $H$  is identified as a synthetic magnetic field along the  $z$ -axis. Notice  $\mathcal{A}_y$  has dimensions of inverse length. Lastly,  $h_x$  represents a Zeeman field along the  $x$ -direction, whose physical origin is a Rabi *spin-flip* term that couples the two internal states of the atom. The vector potential  $\mathcal{A}_y$  may be generated by laser assisted tunneling [1, 2], while the spin-dependent momentum transfer  $k_T$  (spin-orbit) and Zeeman field  $h_x$  may be created via counter-propagating Raman beams [8] or via radio-frequency chips [18].

*Eigenspectrum:* First, we find the eigenspectrum of the Hamiltonian matrix described in Eq. (1) as a function of magnetic flux through a lattice plaquette. We work in a cylindrical geometry having finite number  $N$  of sites along the  $x$ -direction and open boundaries, but periodic boundary conditions along the  $y$ -direction.

In this case, the spin-dependent Harper's matrix

$$\mathbf{H} = \begin{pmatrix} \mathbf{A}_{m-2} & \mathbf{B} & \mathbf{0} & \mathbf{0} & \mathbf{0} \\ \mathbf{B}^* & \mathbf{A}_{m-1} & \mathbf{B} & \mathbf{0} & \mathbf{0} \\ \mathbf{0} & \mathbf{B}^* & \mathbf{A}_m & \mathbf{B} & \mathbf{0} \\ \mathbf{0} & \mathbf{0} & \mathbf{B}^* & \mathbf{A}_{m+1} & \mathbf{B} \\ \mathbf{0} & \mathbf{0} & \mathbf{0} & \mathbf{B}^* & \mathbf{A}_{m+2} \end{pmatrix} \quad (2)$$

has a tridiagonal block structure that couples neighboring sites  $(m-1, m, m+1)$  along the  $x$ -direction and takes full advantage of discrete translational invariance along the  $y$ -axis. The matrices  $\mathbf{A}$ ,  $\mathbf{B}$  and the null matrix  $\mathbf{0}$  consist of  $2 \times 2$  blocks with entries labeled by internal states  $|\uparrow\rangle$  and  $|\downarrow\rangle$ . The size of the space labeled by the site index  $m$  is  $N$ , thus the total dimension of the matrix  $\mathbf{H}$  in Eq. (2) is  $2N \times 2N$ . The matrix indexed by position  $x = ma$  is

$$\mathbf{A}_m = \begin{pmatrix} -2t \cos(k_y a - 2\pi m \alpha) & -h_x \\ -h_x & -2t \cos(k_y a - 2\pi m \alpha) \end{pmatrix},$$

where the parameter  $\alpha = \Phi/\Phi_0$  represents the ratio between the magnetic flux through a lattice plaquette  $\Phi = Ha^2$  and the flux quantum  $\Phi_0 = hc/e$  or the ratio between the plaquette area  $a^2$  and the square of the magnetic length  $\ell_M = hc/eH$ , that is,  $\alpha = (a/\ell_M)^2$ . The matrix containing the spin-orbit coupling is

$$\mathbf{B} = \begin{pmatrix} -te^{-ik_T a} & 0 \\ 0 & -te^{ik_T a} \end{pmatrix}$$

corresponding to momentum shift by  $k_T$  ( $-k_T$ ) along the  $x$ -direction for the  $|\uparrow\rangle$  ( $|\downarrow\rangle$ ) state. Notice that in a cylindrical geometry with open boundaries in the  $x$ -direction, but periodic boundary conditions along the  $y$ -direction,  $k_y$  is a good quantum number, while  $k_x$  is not.

The generalized Hofstadter spectrum can be obtained from the spin-dependent Harper's matrix defined in Eq. (2). We consider the dimensions of the optical lattice to be of fifty (50) sites along the  $x$ -direction, with two spin states per site, but periodic along the  $y$ -direction. The eigenvalues  $E_n(k_y)$  are labeled by a discrete band index  $n$  and by momentum  $k_y$ , and are functions of the spin-orbit coupling  $k_T$ , Zeeman field  $h_x$ , as well as flux ratio  $\alpha = \Phi/\Phi_0$ . In Fig. 1, we show the spectrum of  $\alpha = \Phi/\Phi_0$  versus zero-momentum energy  $E_n(k_y = 0)$  for the following cases: a) zero spin-orbit ( $k_T a = 0$ ) and zero Zeeman field ( $h_x/t = 0$ ), corresponding to the standard *butterfly* graph; b) spin-orbit coupling  $k_T a = \pi/4$  and zero Zeeman field  $h_x/t = 0$  producing the same graph as in a) due to a spin-gauge symmetry that allows gauging away the spin-orbit coupling when  $h_x/t = 0$ ; c) zero spin-orbit coupling ( $k_T a = 0$ ) and Zeeman field  $h_x/t = 1$  producing two Zeeman shifted, but interpenetrating *butterfly* graphs; d) spin-orbit coupling  $k_T a = \pi/4$  and Zeeman field  $h_x/t = 1$  leading to a richer *butterfly-spider* spectrum.

We discuss next the particular case of flux ratio  $\alpha = 1/3$  for the cylindrical geometry described above and analyze the eigenvalues  $E_n(k_y)$  for a few values of spin-orbit parameter  $k_T$  and Zeeman field  $h_x$ . In Fig. 2, we

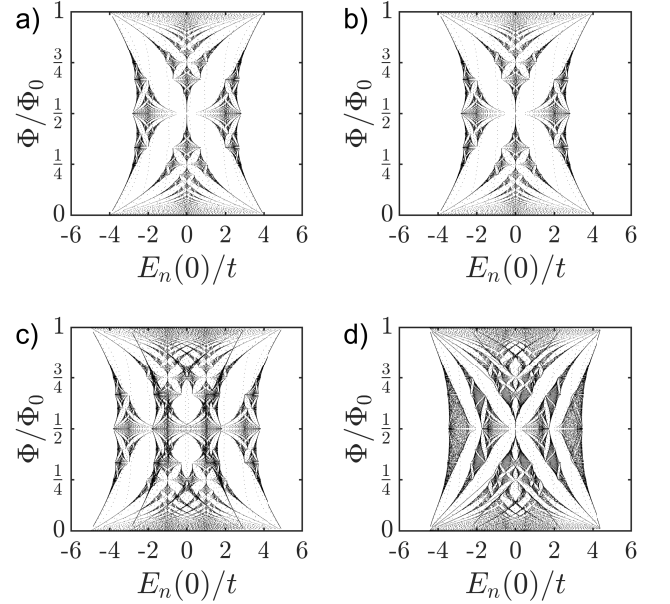


FIG. 1: Flux ratio  $\alpha = \Phi/\Phi_0$  versus energy  $E_n(k_y = 0)$  for various values of spin-orbit coupling parameter  $k_T a$  and Zeeman field  $h_x/t$ . The parameters are: a)  $k_T a = 0$  and  $h_x/t = 0$ , b)  $k_T a = \pi/4$  and  $h_x/t = 0$ , c)  $k_T a = 0$  and  $h_x/t = 1$ , d)  $k_T a = \pi/4$  and  $h_x/t = 1$ .

show the cases: a)  $k_T a = 0$  and  $h_x/t = 0$ , which contains three sets of degenerate bulk bands connected by spin-degenerate edge bands; b)  $k_T a = \pi/4$  and  $h_x/t = 0$ , which is identical to case a) because of a spin-gauge symmetry that allows gauging away the spin-orbit coupling; c)  $k_T a = 0$  and  $h_x/t = 1$  contains six sets of bulk bands because spin-degeneracies are lifted, and spin-dependent edge bands; d)  $k_T a = \pi/4$  and  $h_x/t = 1$ , which contains six sets of bulk bands connected by spin-dependent edge states, all subjected to simultaneous effects of spin-orbit coupling and Zeeman field. Bulk bands in all panels have momentum space period of  $2\pi/3a$ , while the edge bands have period  $2\pi/a$  along the  $k_y$  direction. The periodicity of the bulk states is dictated by the denominator  $q$  of the rational magnetic flux ratio  $\alpha = p/q$ , which for  $\alpha = 1/3$  corresponds to  $p = 1$  and  $q = 3$ . In Fig. 2, the vertical dashed lines indicate the boundaries of the magnetic Brillouin zone at  $k_y a = \pm\pi/3$ .

*Chern numbers:* To study the Chern number spectrum, we convert the cylindrical geometry into a toroidal one, where periodic boundary conditions are imposed along the  $x$  and  $y$  directions. For rational  $\alpha = p/q$ , we write the spin-dependent Harper's Hamiltonian as a  $2q \times 2q$  matrix in momentum  $(k_x, k_y)$  space

$$\mathbf{H}(k_x, k_y) = \begin{pmatrix} \mathbf{H}_{++} & \mathbf{H}_{+-} \\ \mathbf{H}_{-+} & \mathbf{H}_{--} \end{pmatrix} \quad (3)$$

by taking advantage of the magnetic translation group to define  $q \times q$  block matrices  $\mathbf{H}_{ss'}$ , where  $\{s, s'\} = \{\pm, \pm\}$  label spin states  $|\uparrow\rangle = |+\rangle$  and  $|\downarrow\rangle = |-\rangle$ . The spin-

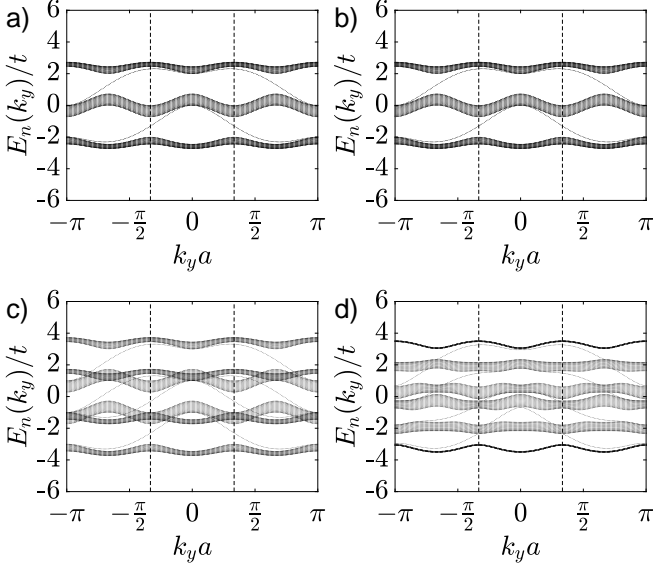


FIG. 2: Eigenvalues  $E_n(k_y)$  of the spin-dependent Harper's matrix versus  $k_y a$  for magnetic flux ratio  $\alpha = 1/3$ . The parameters are: a)  $k_T a = 0$  and  $h_x/t = 0$ , b)  $k_T a = \pi/4$  and  $h_x/t = 0$ , c)  $k_T a = 0$  and  $h_x/t = 1$ , d)  $k_T a = \pi/4$  and  $h_x/t = 1$ . The vertical dashed lines located at  $k_y a = \pm\pi/3$  indicate the boundaries of the magnetic Brillouin zone. The bulk bands have periodicity  $2\pi/3a$ , and the edge bands have periodicity  $2\pi/a$  along the  $k_y$  direction.

diagonal  $q \times q$  block matrices  $\mathbf{H}_{ss}/t$  are

$$\begin{pmatrix} \Gamma_1 & -e^{ik_{xs}a} & 0 & \dots & -e^{-ik_{xs}a} \\ -e^{-ik_{xs}a} & \Gamma_2 & -e^{ik_{xs}a} & \dots & 0 \\ \vdots & \vdots & \vdots & \ddots & \vdots \\ -e^{ik_{xs}a} & 0 & \dots & -e^{-ik_{xs}a} & \Gamma_q \end{pmatrix},$$

where  $k_{xs} = k_x - sk_T$  describes the spin-dependent momentum transfer along the  $x$  direction. The kinetic energy terms are  $\Gamma_m = -2\cos(k_y a - 2\pi\alpha m)$ , with the magnetic flux ratio being  $\alpha = p/q$ , and with  $m$  taking values  $(1, \dots, q)$ . The spin-off-diagonal  $q \times q$  block matrices are

$$\frac{\mathbf{H}_{s\bar{s}}}{t} = \begin{pmatrix} -h_x & 0 & 0 & 0 & 0 \\ 0 & -h_x & 0 & 0 & 0 \\ \vdots & \vdots & \vdots & \ddots & \vdots \\ 0 & 0 & \dots & 0 & -h_x \end{pmatrix}, \quad (4)$$

describing spin-flip processes created by the independently tunable Zeeman field  $h_x$ , with  $\bar{s} = -s$ . The resulting energy spectrum is essentially identical to open boundary problem with cylindrical geometry shown in Fig. 2, except that edge-state energy bands are not present because of the compactification to the toroidal geometry with periodic boundary conditions along the  $x$  and  $y$  directions, that is, in this case there are no edges.

Next, we analyse the Chern spectrum that emerges for arbitrary spin-orbit coupling and Zeeman fields and fixed flux ratio  $\alpha = p/q$ . The energy spectrum associated with the Hamiltonian  $\mathbf{H}(k_x, k_y)$  in Eq. (3) has  $2q$

spin-magnetic bands  $E_{m_\sigma}(\mathbf{k})$  labeled by a magnetic band number  $m_\sigma$  with generalized spin index  $\sigma$ . The minimum number of gaps is  $q-1$  when the bands are doubly degenerate and the maximum number of gaps is  $2q-1$  when there are no degeneracies. In the absence of overlapping regions between the energy bands  $E_{m_\sigma}(\mathbf{k})$ , the Chern index for the  $m_\sigma^{th}$  band with generalized spin index  $\sigma$  is

$$C_{m_\sigma} = \frac{1}{2\pi i} \int_{\partial\Omega} d^2\mathbf{k} F_{xy}^{(m_\sigma)}(\mathbf{k}), \quad (5)$$

where the domain of integration  $\partial\Omega$  corresponds to the magnetic Brillouin zone, that is,  $\partial\Omega_x = [-\pi, \pi]$  and  $\partial\Omega_y = [-\pi/q, \pi/q]$ . The function

$$F_{xy}^{(m_\sigma)}(\mathbf{k}) = \partial_x A_y^{(m_\sigma)}(\mathbf{k}) - \partial_y A_x^{(m_\sigma)}(\mathbf{k}), \quad (6)$$

is the Berry curvature expressed in terms of the Berry connection  $A_j^{(m_\sigma)}(\mathbf{k}) = \langle u_{m_\sigma}(\mathbf{k}) | \partial_j | u_{m_\sigma}(\mathbf{k}) \rangle$  where  $|u_{m_\sigma}(\mathbf{k})\rangle$  are the eigenstates of the Hamiltonian  $\mathbf{H}(k_x, k_y)$  defined in Eq. (3). In the limit of zero spin-orbit coupling ( $k_T = 0$ ) and zero Zeeman field ( $h_x = 0$ ), the energy spectrum for flux ratio  $\alpha = p/q$  has doubly-degenerate  $q$  magnetic bands and  $q-1$  gaps, such that the Chern index from Eq. (5) reduces to the standard form found in the quantum Hall effect literature [19, 20].

To compute the Chern index  $C_{m_\sigma}$ , we generalize a discretization method used in the quantum Hall problem [21] with zero spin-orbit coupling ( $k_T = 0$ ) and zero Zeeman field ( $h_x = 0$ ). We define the link function

$$L_j^{(m_\sigma)}(\mathbf{k}) = \frac{\langle u_{m_\sigma}(\mathbf{k}) | u_{m_\sigma}(\mathbf{k} + \delta\mathbf{k}_j) \rangle}{|\langle u_{m_\sigma}(\mathbf{k}) | u_{m_\sigma}(\mathbf{k} + \delta\mathbf{k}_j) \rangle|} = e^{i\theta_j^{(m_\sigma)}(\mathbf{k})}$$

and obtain the discretized Berry curvature as

$$F_{xy}^{m_\sigma}(\mathbf{k}) = \ln \left[ \frac{L_x^{m_\sigma}(\mathbf{k}) L_y^{m_\sigma}(\mathbf{k} + \delta\mathbf{k}_x)}{L_x^{m_\sigma}(\mathbf{k} + \delta\mathbf{k}_y) L_y^{m_\sigma}(\mathbf{k})} \right], \quad (7)$$

which is a purely imaginary number defined in the range  $-\pi \leq \mathcal{I}[F_{xy}^{m_\sigma}(\mathbf{k})] \leq \pi$ . The Chern index becomes

$$C_{m_\sigma} = \frac{1}{2\pi i} \sum_{\mathbf{k}} F_{xy}^{(m_\sigma)}(\mathbf{k}). \quad (8)$$

When the energy bands  $E_{m_\sigma}(\mathbf{k})$  overlap, that is, there are residual degeneracies in momentum space, we need to redefine the link variable of the degenerate bundle with degeneracy  $D$  via the multiplet  $|\psi_{m_\sigma}^{(D)}(\mathbf{k})\rangle = [|u_{m_\sigma}^{(1)}(\mathbf{k})\rangle, \dots, |u_{m_\sigma}^{(D)}(\mathbf{k})\rangle]$ , leading to

$$L_j^{(m_\sigma)}(\mathbf{k}) = \frac{\text{Det} \langle \psi_{m_\sigma}^{(D)}(\mathbf{k}) | \psi_{m_\sigma}^{(D)}(\mathbf{k} + \delta\mathbf{k}_j) \rangle}{|\text{Det} \langle \psi_{m_\sigma}^{(D)}(\mathbf{k}) | \psi_{m_\sigma}^{(D)}(\mathbf{k} + \delta\mathbf{k}_j) \rangle|} = e^{i\theta_j^{(m_\sigma)}(\mathbf{k})}$$

with these new definitions, the expression for the Berry curvature defined in Eq. (7) remains valid when written in terms of the new link functions defined above. For two internal states and magnetic flux ratio  $\alpha = p/q$ , there is

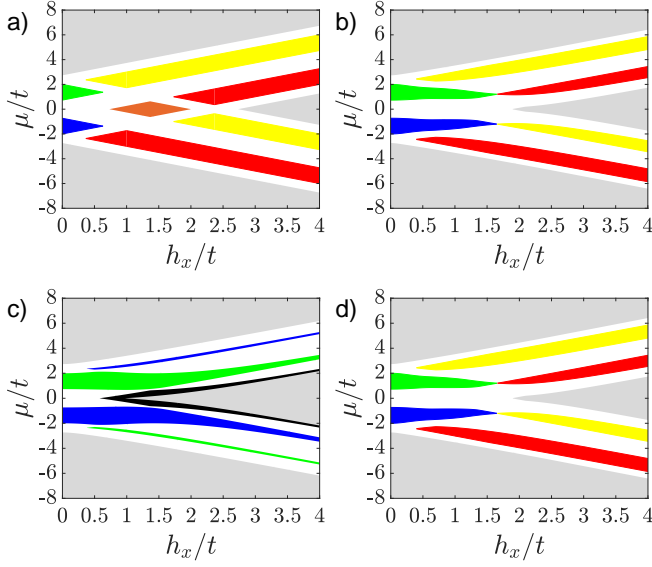


FIG. 3: (Color Online) Phase diagrams of chemical potential  $\mu$  versus Zeeman field  $h_x$  and the associated Chern number spectrum are shown for spin-orbit coupling parameters: a)  $k_T a = 0$ , b)  $k_T a = \pi/4$ , c)  $k_T a = \pi/2$ , and d)  $k_T a = 3\pi/4$ . The white regions correspond to conducting phases and the non-white regions of different colors correspond to insulating phases. The values of the Chern numbers for each colored region are +2 (blue), +1 (red), 0 (gray, black, orange), -1 (yellow), -2 (green). The gray regions are topologically trivial with no edge states, the black regions are topologically trivial with non-chiral edge states, and the orange regions are topologically non-trivial having two edge states with opposite chirality characteristic of quantum spin-Hall (QSH) phases.

a maximum of  $2q$  non-overlapping bands and a maximum of  $2q$  Chern indices.

Chern indices are properties of bands  $E_{m\sigma}(\mathbf{k})$  or band bundles with degeneracy  $D$  and are independent of the location of the chemical potential  $\mu$ . However, Chern numbers are defined only within band gaps and their values dependent on which gap the chemical potential is located. If the chemical potential  $\mu$  is located in a band gap corresponding to filling factor  $\nu = r/q$ , then the Chern number at this value of  $\mu$  is the sum of Chern indices of bands with energies  $E < \mu$ .

$$C_r = \sum_{m\sigma, E < \mu}^{\nu=r/q} C_{m\sigma}. \quad (9)$$

Furthermore, via the bulk-edge correspondence [22], the Chern number  $C_r$  calculated from the toroidal geometry (bulk system without edges) measures the total chirality of edge states that are present in the gap for the cylindrical geometry.

**Phase Diagrams:** In Fig. 3, we show the phase diagram of chemical potential  $\mu$  versus Zeeman field  $h_x$  for fixed value of the magnetic flux ratio  $\alpha = 1/3$  and four values of the spin-orbit parameter: a)  $k_T a = 0$ , b)  $k_T a = \pi/4$ , c)  $k_T a = \pi/2$ , and d)  $k_T a = 3\pi/4$ . The white

regions indicate conducting phases, while the other colors indicate insulating phases with Chern numbers +2 (blue), +1 (red), 0 (gray, black, orange), -1 (yellow), -2 (green). The gray regions are topologically trivial with no edge states, the black regions are topologically trivial with non-chiral edge states, while the orange region is topologically non-trivial having two edge states with opposite chirality characteristic of a quantum spin-Hall (QSH) phase. For fixed magnetic flux  $\alpha = 1/3$ , the number of insulating phases between conducting regions increases from two (2) at low Zeeman fields to five (5) at high Zeeman fields. This does not occur in electronic systems, because the Zeeman field  $h_x$  cannot be tuned independently of the magnetic ratio  $\alpha$ , and typically has very small values in comparison to the hopping parameter  $t$ , such that  $h_x/t \ll 1$ . However, for ultra-cold fermions,  $h_x$  is a synthetic field that can be tuned independently of the magnetic ratio  $\alpha$  and can attain high values in comparison to  $t$ .

The Chern number spectrum is odd under inversion through filling factor  $\nu = 1$  (around  $\mu = 0$ ), as can be seen in all panels of Fig. 3. Furthermore, the Chern number spectrum is even under inversion through  $k_T a = \pi/2$ , therefore it is the same for  $k_T a = \pi/4$  and  $k_T = 3\pi/4$ , as seen in Fig. 3b and Fig. 3d. The lower and upper gray regions in all panels of Fig. 3 correspond to trivial insulating phases with filling factors  $\nu = 0$  and  $\nu = 2$ , respectively. In all insulating regions the system is incompressible, that is,  $d\nu/d\mu = 0$ .

In Fig. 3a, there is one insulating phase with filling factor  $\nu = 1/3$  (lower red region), two insulating phases with  $\nu = 2/3$  (blue and lower yellow region), two insulating phases with  $\nu = 1$  (orange and central gray region), two insulating phases with  $\nu = 4/3$  (green and upper red region), and one insulating phase with  $\nu = 5/3$  (upper yellow region). The most interesting feature of Fig. 3a is the orange region around  $\mu = 0$  with filling factor  $\nu = 1$ , which exhibits the QSH effect. In Fig. 3b essentially the same phases of Fig. 3a are present, except for the orange region which disappears, because the spin-orbit parameter  $k_T a$  is too large to preserve edge states with opposite chirality. The most interesting feature of Fig. 3b is the direct topological quantum phase transitions between the blue ( $C_2 = +2$ ) and an yellow ( $C_2 = -1$ ) regions at filling factor  $\nu = 2/3$  and between the green ( $C_4 = -2$ ) and red ( $C_4 = +1$ ) regions at  $\nu = 4/3$ , where two chiral edge states disappear as the gap closes and a single chiral edge of opposite chirality emerges as the gap reopens. In Fig. 3c, where  $k_T a = \pi/2$ , there are only insulating phases with even Chern numbers: the lower green region ( $C_1 = -2$ ) at  $\nu = 1/3$ , the lower blue region ( $C_2 = +2$ ) at  $\nu = 2/3$ , the central gray and black regions ( $C_3 = 0$ ) at  $\nu = 1$ , the upper green region ( $C_4 = -2$ ) at  $\nu = 4/3$ , and the upper blue region ( $C_5 = +2$ ) at  $\nu = 5/3$ . In Fig. 3d, where  $k_T a = 3\pi/4$ , the phases shown are identical to those of Fig. 3b, where  $k_T a = \pi/4$ , because the Chern spectrum is even under inversion through  $k_T a = \pi/2$ .

The number and type of insulating states discussed



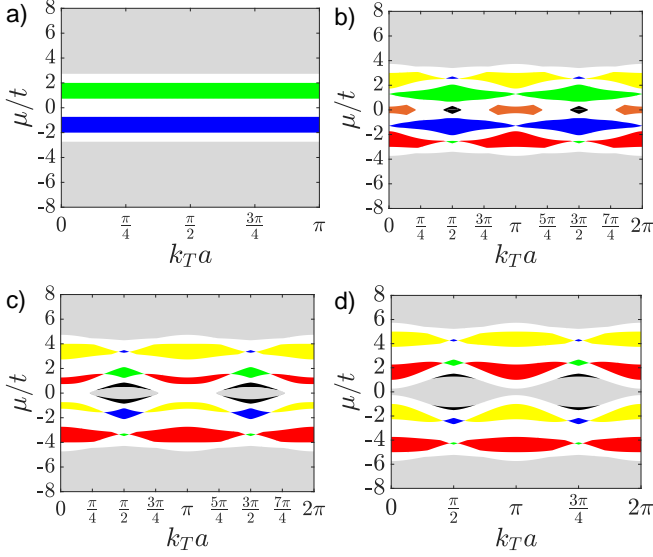


FIG. 4: (Color Online) Chemical potential  $\mu/t$  versus spin-orbit parameter  $k_T a$  for flux ratio  $\alpha = 1/3$  and Zeeman fields: a)  $h_x/t = 0$ , b)  $h_x/t = 1$ , c)  $h_x/t = 2$ , d)  $h_x/t = 3$ . The color code for the Chern numbers is the same as in Fig. 3.

here are very different from those of the integer quantum Hall effect found in semiconductor physics, when  $h_x = 0$  and  $k_T = 0$ . For  $\alpha = 1/3$ , there are only two possibilities for the Chern number:  $C_2 = +2$  at  $\nu = 2/3$  and  $C_4 = -2$  at  $\nu = 4/3$ , when  $h_x = 0$  and  $k_T = 0$ . However, as  $h_x$  is varied for fixed  $k_T$  new topological insulating phases emerge with additional Chern numbers and filling factors. For a fixed magnetic ratio  $\alpha = p/q$ , the index  $r$  labels gaps in the energy spectrum  $E_{m_\sigma}(\mathbf{k})$  and is related to the integers  $p$  and  $q$  via the Diophantine equation  $r = qS_r + pC_r$ , where  $S_r$  is a supplementary topological invariant and  $C_r$  is the Chern number. This relation can be rewritten in terms of the filling factor  $\nu = r/q$  and the magnetic ratio  $\alpha = p/q$  as

$$\nu = S_r + \alpha C_r. \quad (10)$$

Notice that  $r$  can take a maximum value of  $2q$ , when  $\nu = 2$ . For  $\alpha = 1/3$ , incompressible phases with filling factors  $\nu = 0$  ( $r = 0$ ) and  $\nu = 2$  ( $r = 6$ ) have Chern numbers  $C_0$  and  $C_6$  trivially equal to zero, therefore  $S_r$  can only take non-negative integer values  $0, 1, 2$ , as  $r$  varies from 0 to 6. The relation shown in Eq. (10) generalizes the gap-labeling theorem [23, 24] used in the context of the integer quantum-Hall effect, because the topological quantum numbers  $(S_r, C_r)$  change not only as a function of the magnetic ratio  $\alpha$ , but also as a function of the Zeeman field  $h_x/t$  and spin-orbit parameter  $k_T a$ .

In Fig. 4, we show the phase diagram of chemical potential  $\mu/t$  versus spin-orbit parameter  $k_T a$  illustrating all the insulating phases for magnetic ratio  $\alpha = 1/3$  and changing Zeeman fields: a)  $h_x/t = 0$ , b)  $h_x/t = 1$ , c)  $h_x/t = 2$  and d)  $h_x/t = 3$ . The color code for insulating phases is the same used in Fig. 3. Notice that the

Chern spectrum is periodic in  $k_T a$  with period equal to  $\pi$ , and that topological quantum phase transitions between insulators with different Chern numbers occur as  $k_T a$  is changed for fixed  $h_x/t$ . The lower and upper gray regions correspond to  $\nu = 0$  with  $(S_0, C_0) = (0, 0)$ , and  $\nu = 2$  with  $(S_6, C_6) = (2, 0)$ .

In Fig. 4a, where  $h_x/t = 0$ , there are only two topological insulating phases. The first one is the blue region at  $\nu = 2/3$  with  $(S_2, C_2) = (0, +2)$ , and the second is the green region at  $\nu = 4/3$ , with  $(S_4, C_4) = (2, -2)$ . Because of the spin-gauge symmetry at  $h_x/t = 0$ , the values of  $(S_r, C_r)$  are independent of the spin-orbit coupling parameter  $k_T a$ . In Fig. 4b, where  $h_x/t = 1$ , more topological insulating phases emerge at additional filling factors. At  $\nu = 1/3$  there is a red region with  $(S_1, C_1) = (0, +1)$  and a green region with  $(S_1, C_1) = (1, -2)$ . At  $\nu = 2/3$  there is a blue region with  $(S_2, C_2) = (0, +2)$ . At  $\nu = 1$  there are orange and black regions with  $(S_3, C_3) = (1, 0)$ . At  $\nu = 4/3$  there is a green region with  $(S_4, C_4) = (2, -2)$ . At  $\nu = 5/3$  there is a yellow region with  $(S_5, C_5) = (2, -1)$  and a blue region with  $(S_5, C_5) = (1, +2)$ . Similar topological indexing can be done for Figs. 4c and 4d, with the most important differences from Fig. 4b being the emergence of yellow regions at  $\nu = 2/3$  with  $(S_2, C_2) = (1, -1)$ , gray regions at  $\nu = 1$  with  $(S_3, C_3) = (1, 0)$ , and red regions at  $\nu = 4/3$  with  $(S_4, C_4) = (1, +1)$ . Notice that the topologically non-trivial orange region (QSH insulator) of Fig. 4b disappears at larger Zeeman fields in Fig. 4c ( $h_x/t = 2$ ) and Fig. 4d ( $h_x/t = 3$ ), as particle-like and hole-like magnetic bands no longer overlap, such that edge states with opposite chirality disappear leaving either non-chiral edge states or no edge states at all.

Finally, notice a staircase structure of the filling factor  $\nu$  versus chemical potential  $\mu$  both in Fig. 3 for fixed Zeeman field  $h_x/t$  and in Fig. 4 for fixed spin-orbit coupling  $k_T a$ . The steps of this staircase occur at values of  $\nu$  given by the Diophantine relation in Eq. (10).

*Conclusions:* We have discussed the Chern number spectrum of ultra-cold fermions in square optical lattices as a function of artificial magnetic, Zeeman and spin-orbit fields that can be tuned independently. As a specific example, we obtained phase diagrams of chemical potential versus Zeeman and spin-orbit fields for fixed magnetic flux ratio  $\alpha = 1/3$ . We showed that Chern numbers are dramatically modified when Zeeman and spin-orbit fields are changed for fixed magnetic field, and that topological quantum phase transitions between different insulating states are induced by Zeeman and spin-orbit fields at fixed filling factor. Lastly, we obtained a staircase structure in the filling factor versus chemical potential for changing Zeeman and spin-orbit fields, showing the existence of incompressible states at rational filling factors obtained from a generalized Diophantine equation.

One of us (C.A.R.S.d.M.) would like to thank the support of the Galileo Galilei Institute for Theoretical Physics via a Simons Fellowship, and of the International Institute of Physics via the Visitor's Program.

- 
- [1] M. Aidelsburger, M. Atala, M. Lohse, J. T. Barreiro, B. Paredes, and I. Bloch, Realization of the Hofstadter Hamiltonian with Ultracold Atoms in Optical Lattices, *Phys. Rev. Lett.* **111**, 185301 (2013).
  - [2] Hirokazu Miyake, Georgios A. Siviloglou, Colin J. Kennedy, William Cody Burton, and Wolfgang Ketterle, Realizing the Harper Hamiltonian with Laser-Assisted Tunneling in Optical Lattices *Phys. Rev. Lett.* **111**, 185302 (2013).
  - [3] K. von Klitzing, G. Dorda, and M. Pepper, New Method for High-Accuracy Determination of the Fine-Structure Constant Based on Quantized Hall Resistance, *Phys. Rev. Lett.* **45**, 494 (1980).
  - [4] D. C. Tsui, H. L. Stormer, and A. C. Gossard, Two-Dimensional Magnetotransport in the Extreme Quantum Limit, *Phys. Rev. Lett.* **48**, 1559 (1982).
  - [5] P. G. Harper, Single Band Motion of Conduction Electrons in a Uniform Magnetic Field, *Proc. Phys. Soc. London Sect. A* **68**, 874 (1955).
  - [6] D. R. Hofstadter, Energy levels and wave functions of Bloch electrons in rational and irrational magnetic fields, *Physical Review B* **14**, 2239-2249 (1976).
  - [7] M. Aidelsburger, M. Lohse, C. Schweizer, M. Atala, J. T. Barreiro, S. Nascimbene, N. R. Cooper, I. Bloch and N. Goldman, Measuring the Chern number of Hofstadter bands with ultracold bosonic atoms, *Nature Phys.* **11**, 162 (2014).
  - [8] Y. J. Lin, K. Jimenez-Garcia, and I. B. Spielman, Spin-orbit coupled Bose-Einstein condensates, *Nature (London)* **471**, 83 (2011).
  - [9] C. L. Kane and E. J. Mele,  $Z_2$  Topological Order and the Quantum Spin Hall Effect, *Phys. Rev. Lett.* **95**, 146802 (2005).
  - [10] L. Sheng, D. N. Sheng, C. S. Ting, and F. D. M. Haldane Nondissipative Spin Hall Effect via Quantized Edge Transport, *Phys. Rev. Lett.* **95**, 136602 (2005).
  - [11] B. A. Bernevig and S.-C. Zhang, Quantum Spin Hall Effect, *Phys. Rev. Lett.* **96**, 106802 (2006).
  - [12] N. Fläschner, B. S. Rem, M. Tarnowski, D. Vogel, D.-S. Lühmann, K. Sengstock and C. Weitenberg, Experimental reconstruction of the Berry curvature in a Floquet Bloch band, *Science* **352**, 1091 (2016).
  - [13] E. Zhao, N. Bray-Ali, C. J. Williams, I. B. Spielman, and I. I. Satija, Chern numbers hiding in time-of-flight images, *Phys. Rev. A* **84**, 063629 (2011).
  - [14] P. Hauke, M. Lewenstein and A. Eckardt, Tomography of Band Insulators from Quench Dynamics, *Phys. Rev. Lett.* **113**, 045303 (2014).
  - [15] G. Jotzu, M. Messer, R. Desbuquois, M. Lebrat, T. Uehlinger, D. Greif and T. Esslinger, Experimental realization of the topological Haldane model with ultracold fermions, *Nature* **515**, 237 (2014).
  - [16] H. M. Price, and N. R. Cooper, Mapping the Berry curvature from semiclassical dynamics in optical lattices, *Phys. Rev. A* **85**, 033620 (2012).
  - [17] A. Dauphin, N. Goldman, Extracting the Chern number from the dynamics of a Fermi gas: implementing a quantum Hall bar for cold atoms, *Phys. Rev. Lett.* **111**, 135302 (2013).
  - [18] N. Goldman, I. Satija, P. Nikolic, A. Bermudez, M. A. Martin-Delgado, M. Lewenstein, and I. B. Spielman, Realistic Time-Reversal Invariant Topological Insulators with Neutral Atoms, *Phys. Rev. Lett.* **105**, 255302 (2010).
  - [19] D. J. Thouless, M. Kohmoto, M. P. Nightingale, and M. den Nijs, Quantized Hall Conductance in a Two-Dimensional Periodic Potential, *Phys. Rev. Lett.* **49**, 405-408 (1982).
  - [20] M. Kohmoto, Topological Invariant and the Quantization of the Hall Conductance, *Ann. Phys.* **160**, 343 (1985).
  - [21] T. Fukui, Y. Hatsugai and H. Suzuki, Chern Numbers in Discretized Brillouin Zone: Efficient Method of Computing (Spin) Hall Conductances, *J. Phys. Soc. Jpn.* **74**, 1674 (2005).
  - [22] Y. Hatsugai, Topological aspects of the quantum Hall effect, *J. Phys.: Condens. Matter* **9**, 2507 (1997).
  - [23] G. H. Wannier, A Result Not Dependent on Rationality for Bloch Electrons in a Magnetic Field, *Phys. Stat. Sol. (b)* **88**, 767 (1978).
  - [24] F. H. Claro and G. H. Wannier, Magnetic subband structure of electrons in hexagonal lattices, *Phys. Rev. B* **19**, 6068 (1979).
  - [25] N. Goldman, J. Dalibard, A. Dauphin, F. Gerbier, M. Lewenstein, P. Zoller, I. B. Spielman, Direct imaging of topological edge states in cold-atom systems, *Proc. Natl. Acad. Sci. U.S.A.* **110**, 6736 (2013).
  - [26] Y.-J. Lin, R. L. Compton, K. Jimenez-Garcia, J. V. Porto and I. B. Spielman, Synthetic magnetic fields for ultracold neutral atoms, *Nature* **462**, 628 (2009).